IEEE Access
Multidisciplinary | Rapid Review | Open Access Journal

Received May 24, 2020, accepted June 7, 2020, date of publication June 12, 2020, date of current version June 26, 2020.

Digital Object Identifier 10.1109/ACCESS.2020.3001947

Optimal Design of Sparse Array for Ultrasonic Total Focusing Method by Binary Particle Swarm Optimization

HAN ZHANG[1], BICHAO BAI[2], JIANFENG ZHENG[2], AND YUN ZHOU[2]
[1]Key Laboratory of Noise and Vibration, Institute of Acoustics, Chinese Academy of Sciences, Beijing 100190, China
[2]School of Mechanical Engineering, Changzhou University, Changzhou 213164, China

Corresponding author: Han Zhang (zhanghan@mail.ioa.ac.cn)

This work was supported in part by the National Natural Science Foundation of China under Grant 11772349 and Grant 11972354.

ABSTRACT Ultrasonic phased array technology is used in various fields. Traditional full phased arrays place elements in every position of a uniform lattice with half-wavelength spacing between the lattice points, so the hardware cost is very high. This paper introduces an automatically method to sparsify the full array method with well-controlled sidelobes and the main lobe. By calculating one-dimensional phased array patterns that can reflect phased array performance, the binary particle swarm optimization (BPSO) algorithm is used to optimize the array layout. The method initialized form full array and decreased several elements step by step, then, a sparse array with comprehensive acoustic performance close to the reference full array is obtained. By applying the proposed method to the sparse array design of total focusing method (TFM), the simulation results indicate that the proposed sparse total focusing method can greatly increase computational efficiency while providing significantly higher image quality. The BPSO can provide effective optimization design for sparse arrays.

INDEX TERMS Binary particle swarm optimization, sparse array, total focusing method, ultrasonic phased array.

I. INTRODUCTION

The phased array technology originated from the advanced phased array radar technology, which is widely used in marine landform detection and advanced anti-submarine sonar. In phased array radar technology, a large number of sub-antenna arrays are arranged according to a certain rule or shape combination, and then by controlling the delay and amplitude of the electromagnetic beam emitted by each sub-array, a flexible and variable radar focus can be formed within a certain time and space beam. Ultrasonic phased array is a transducer array composed of several piezoelectric transducer elements. Its basic function is to realize phase-control transmission or reception of ultrasonic waves.

In the early stage, the ultrasonic phased array was mainly used in the medical field. In medical ultrasound imaging, the phased array transducer was used to quickly move the sound beam to image the organ to be examined [1]. In ultrasound therapy, ultrasonic phased array allows one to vary the position of the focusing area without mechanical movement of the array itself, and to create several focal at the same time [2]. High-intensity focused ultrasound technique can make the ultrasound energy highly concentrated in the deep tissues of the human body, thereby causing acute thermal damage to the diseased tissue in a short time without affecting the surrounding normal tissues [3]. Nowadays, various High-intensity focused ultrasound array transducers have been developed and applied in a wide range of medical fields to ablate various types of lesions [2], [4]. Further, the application of ultrasonic phased array in the field of micro-manipulation has shown initial effects. In 2015, Marzo et al proposed the acoustic holography technology to manufacture dynamic Wells to flexibly manipulate suspended particles [5]. However, the presence of beam sidelobes in the ultrasonic phased array reduces the performance of the phased array in its corresponding application field. For example, the damage to normal tissues during high-intensity focused ultrasound treatment or the decline of imaging quality in ultrasound diagnosis.

With the development of piezoelectric materials and computers, phased array technology has also gradually been applied to industrial inspection, and has made considerable

The associate editor coordinating the review of this manuscript and approving it for publication was Yanbo Chen.

development and extensive applications in the nuclear industry, aerospace, oil and gas pipelines, and other fields [6]. The total focusing method (TFM) uses full array acquisition, which means that a single array element excites all array elements to receive, and each array element sequentially fires until all the combination of excitation and reception is used to obtain complete detection information. In the post-processing phase, various phased sound beams are reconstructed through flexible delay settings, to achieve focused imaging at any position in the inspection area [7]. However, to obtain a smaller main beam width, a modern high-resolution ultrasonic phased array detection system requires a larger aperture of the transducer array. At the same time, to prevent the appearance of grating lobes, the element spacing must not be greater than half the wavelength. Therefore, the number of array elements required for high-resolution phased arrays is high, and the hardware cost is extremely high. Moreover, due to a large amount of complete matrix data, the calculation of TFM is very time-consuming, which limits its application in certain industrial fields, especially for the case of high real-time detection requirements. The research to improve the performance of the ultrasonic phased array system has been the main issue in recent years.

Previous research has shown that the sparse array can provide an effective method to solve this problem [1], [8]. The sparse array not only can reduce the cost and weight of the array, but also obtain a narrow beam equivalent to the full array arrangement. When the array elements are excited with equal amplitude, the sparse array can obtain a lower sidelobe level than the full array. For TFM, because of the time delay of the ultrasonic wave propagation, there should be a minimum time interval between two firings, which results in time burdens of acquisition. The sparse array approach can also save the acquisition time. Peng *et al.* [9] increased the array aperture to shorten the time for TFM calculation, but the unified sparse array method used does not consider the effect of element layout on array performance. To improve the spatial resolution of the image and reduce artifacts of phased array imaging, applying simulated annealing [10] and genetic algorithm (GA) [11] to array element layout optimization can produce good results in small-scale sparse array optimization. Bray *et al.* [12] used a genetic GA to optimize the element layout of the linear sparse phased array, however, because of the sound field characteristics of the sparse array are not considered, the effective aperture of the sparse array and that of the full array are inconsistent, thereby affecting the imaging performance of the sparse array. Yang *et al.* [13] optimized the two-dimensional random sparse array by combining the GA and the minimum redundancy method, and solved the problem of poor consistency of the sparse array, but did not consider the change of the acoustic radiation pattern. Lockwood *et al.* [14] proposed the concept of effective aperture, using a redefinition function to correct the sparse array to obtain a sound field characteristic similar to the full array. However, the optimization of the sparse space layout was not considered.

This paper proposes an optimized design method for the sparse array. By calculating the array beam directivity diagram, the element layout of the sparse array is optimized by binary particle swarm optimization (BPSO). i.e. removed some elements from the reference full array by minimizing the fitness value. Unlike previous sparse array research, this paper does not need to set the sparse rate of the target sparse array and can finally achieve a balance between array performance and sparse rate. Simulation results show that the optimized sparse array has better sound field characteristics. We use the optimized sparse array for TFM, the results show that its imaging resolution is close to that of the reference full array, with few sidelobe artifacts, high image signal noise ratio (SNR), and less imaging time consumption. The proposed method is so universal that the full array of any number of array elements can use the proposed algorithm to improve the performance of a phased array. The proposed method can be applied to sparse phased array design in many fields. For example, the proposed method will apply to TFM in the industrial ultrasonic testing, further improve imaging quality and real-time testing efficiency based on [15], [16].

The rest of the paper is organized as follows: Section II presents the details of the core idea of FMC and TFM technology, further, we elaborate the method of optimizing the element layout of the linear sparse phased array by BPSO. Section III presents the optimization results of arrays, then the optimized sparse array performance was tested by comparison of TFM simulation results. Section IV concludes the paper.

II. THEORY

A. FULL FOCUS ALGORITHM MODEL

The Full Matrix Capture (FMC) is an advanced data acquisition method based on array transducers. As shown in Fig. 1, the FMC excites on a single array element, and all array elements receive at the same time, which is performed in sequence until all the excitation and reception combinations are obtained, and then complete detection information is obtained.

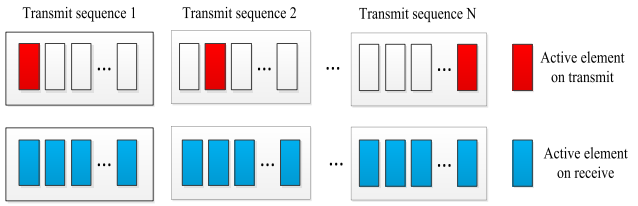

FIGURE 1. Schematic illustration of the method used for calculations.

A one-dimensional linear array probe considering N array elements is placed on the surface of a two-dimensional isotropic homogeneous medium, and point defects are located inside the medium. Establish a two-dimensional coordinate system Oxz, as shown in Fig. 2.

The x-axis is along the array direction and parallel to the surface of the medium. The z-axis is perpendicular to the surface of the medium and points to the inside of the medium.

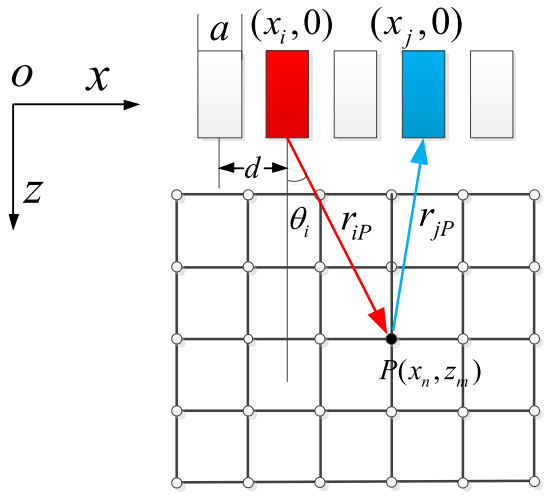

FIGURE 2. A schematic diagram of two dimensional Total Focusing Method geometric model.

The array is arranged on the x-axis, and the imaging area is below the array. Assuming that the number of array elements is N and the echo received at the center point of each array element is recorded as $u(x_i, x_j, t)$, the data collected by the full matrix is a three-dimensional matrix, as shown in (1).

$$u(x_i, x_j, t) = \begin{Bmatrix} u(x_1, x_1, t), & u(x_1, x_2, t) & \cdots & u(x_1, x_N, t) \\ u(x_2, x_1, t), & u(x_2, x_2, t) & \cdots & u(x_2, x_N, t) \\ & & \vdots & \\ u(x_N, x_1, t) & u(x_N, x_2, t) & \cdots & u(x_N, x_N, t) \end{Bmatrix} \tag{1}$$

where $i, j = 1, 2, \ldots N$, x_i and x_j denote the coordinates of the excitation and receiving elements, respectively, and t is time. There is a scattering point $P(x_n, z_m)$ below the array, where $n = 1, 2, \ldots, M1, m = 1, 2, \ldots M2.M1$ is the number of pixels in the x-direction in the imaging area, $M2$ is the number of pixels in the z-direction in the imaging area. According to the geometric relationship of Fig. 2, the distances from the excitation element $(x_i, 0)$ and the receiving element $(x_j, 0)$ to the scattering point $P(x_n, z_m)$ are given by

$$r_{iP} = \sqrt{(x_i - x_n)^2 + z_m^2} \tag{2}$$

$$r_{jP} = \sqrt{(x_j - x_n)^2 + z_m^2} \tag{3}$$

Then, the i^{th} element is excited, and after reflecting at the focal point $P(x_n, z_m)$, the acoustic propagation delay t_{ijp} when it is received by the j^{th} element can be denoted as

$$t_{ijP} = \frac{r_{iP} + r_{jP}}{c} = \frac{\sqrt{(x_i - x_n)^2 + z_m^2} + \sqrt{(x_j - x_n)^2 + z_m^2}}{c} \tag{4}$$

where c is the longitudinal velocity of sound. In Fig.2, the pixel intensity value $I(x_n, z_m)$ of any imaging point $P(x_n, z_m)$ can be expressed as

$$I(x_n, z_m) = \sum_{i=1}^{N}\sum_{j=1}^{N} h(x_i, x_j, t_{ijP}) = \sum_{i=1}^{N}\sum_{j=1}^{N} h_{ij}\left(\frac{r_{iP} + r_{jP}}{c}\right) \tag{5}$$

where h_{ij} is the analytical version of the echo received signal.

B. BEAM DIRECTIVITY OF THE SPARSE ARRAY

It can be seen from (1) and (5) that TFM pixel synthesis needs to process a large amount of data information, which increases the processing time of the processor and reduces the frame rate of real-time imaging. The sparse array can make the performance of the sparse-TFM as close to the full array as possible while reducing the array elements. Although the number of effective array elements of the sparse array is reduced, due to the sparse arrangement of the array element position, the grating lobes are eliminated. And because its effective aperture can be the same as a full array, so they have a similar mainlobe characteristic, i.e. nearly the same lateral resolution [9]. To get the performance index that can evaluate the sparse array, we established an optimization model firstly. For a linear array as shown in Fig.1, the sound pressure of a single element can be defined as [17]

$$p(r, \theta, t) = \left(\frac{p_0}{r}\right)^{1/2} \frac{\sin(ka \sin\theta/2)}{ka \sin\theta/2} \exp(j(\omega t - kr)) \tag{6}$$

where r is the distance between the imaging point and the array element, k is the wavenumber, θ is the direction angle, ω is the circular frequency, a is the element width. For the sparse array, the synthesized sound pressure can be defined as

$$p(r, \theta, t) = \sum_{i=1}^{N} g_i p_i(r, \theta, t) \tag{7}$$

where g_i is the binary coefficient, g_i is 1 denotes the i^{th} element is active and g_i is 0 denotes it is inactive. Then we can get the beam directivity function under the sparse array distribution by

$$H(\theta) = \left|\frac{p(r, \theta, t)}{p(r, \theta_m, t)}\right| \tag{8}$$

where, θ_m is the steering angle of the phased array, which is set to 0 here. The directivity diagram of a sparse array can reflect the imaging performance of the array. Hence, we can optimize the array according to the characteristics of the directivity diagram.

C. OPTIMIZATION PROBLEM FORMULATION

Because the particle swarm algorithm has the characteristics of simple operation steps, easy programming, high search efficiency, and wide applicability. And the algorithm can face the problem to be solved, it reduces the coding and decoding process of the problem solution in the genetic algorithm, which is very suitable for the optimization of constraint problems [18], [19].

We aim to reduce the number of effective array elements to reduce the calculation time of TFM, at the same time, we want to guarantee the SNR and resolution of the imaging. Therefore, our optimization objectives are the contrast resolution and spatial resolution of the sparse array. The contrast resolution and spatial resolution can be characterized by the maximum sidelobe level (MSL) and the -6 dB width of the mainlobe of the directivity diagram of a sparse array, respectively [11]. The sparse array directivity diagram can be obtained by (8). Since the main-lobe width (MLW) and MSL cannot be perfect optimized simultaneously perfectly in the directivity diagram, we define the fitness function as follows

$$Fit = \psi_1 * MSL + \psi_2 * MLW \tag{9}$$

where, ψ_1 and ψ_2 are coefficient values selected according to different optimization objectives. Since we want to take into account the characteristics of both the mainlobe and sidelobes, both ψ_1 and ψ_2 are set to 1.

This paper is to optimize the element layout of the linear sparse phased array by minimizing the fitness value. That is, each array element is first placed at equal intervals according to grating lobe suppression rule, then based on reference full array, some array elements are closed by minimizing the objective function to achieve the purpose of the sparse array. Finally, a sparse array of the combined good performance of the MSL and MLW of the beam can be obtained. The optimization of the full array means the optimization of the parameter g_i, for $i = 1, 2, \cdots, N$. g_i is a binary parameter. Therefore, this paper uses a BPSO as the optimization method of the one-dimensional sparse array. Each particle carries a binary code of dimension N, which indicates the distribution of the N array element. The value of the k^{th} dimension of the j^{th} particle after the t^{th} iteration is updated by

$$Y_{jk}(t+1) = g_i \tag{10}$$

Particle velocity update formula is given by

$$v_{jk}(t+1) = \omega(t) \cdot v_{jk}(t) + c_1 R_{1k}(t)[Y_P - Y_{jk}(t)] + c_2 R_{2k}(t)[Y_G - Y_{jk}(t)] \tag{11}$$

where c_1 and c_2 are acceleration factors both equalling to 2, $Y_{jk}(t)$ and $v_{jk}(t)$ represent the position and velocity of the k^{th} dimension of the j^{th} particle at the t^{th} iteration, respectively. $R_{1k}(t)$ and $R_{2k}(t)$ are uniformly-distributed random numbers between 0 and 1. Y_P and Y_G are personal best and global best, respectively. w is the inertia coefficient, and its value changes with the number of iterations, which is given by

$$w(t) = w_{\max} - (w_{\max} - w_{\min})\frac{t}{T_{\max}} \tag{12}$$

where, $w_{\max}$ and $w_{\min}$ are the maximum and minimum inertia coefficients, respectively. $T_{\max}$ represents the maximum number of iterations. In this way, the particle velocity can be controlled and premature convergence can be avoided. To optimize the BPSO algorithm, we set $w_{\max} = 0.9$, $w_{\min} = 0.4$. In order to control the global search behavior of particles, the particle speed is clamped in a bounded range. A positive integer $v_{\max}$ is introduced so that $v_{jk}(t)$ satisfies

$$v_{jk}(t+1) \begin{cases} v_{\max}, & \text{if } v_{jk}(t+1) > v_{\max} \\ -v_{\max}, & \text{if } v_{jk}(t+1) < -v_{\max} \\ v_{jk}(t+1), & \text{otherwise} \end{cases} \tag{13}$$

If the speed converges to close near $v_{\max}$ or $-v_{\max}$, it will be hard to change the corresponding position at a small change of velocity, which makes it difficult to escape from the good local optimal value of BPSO. To solve this problem, we introduce the following operation after the velocity update (13).

$$v_{jk}(t+1) \begin{cases} l - v_{jk}(t+1), & \text{if } R_{3k}(t) < r_{\text{mu}} \\ v_{jk}(t+1), & \text{otherwise} \end{cases} \tag{14}$$

where $R_{3k}(t)$ indicates the random number between 0 and 1. r_{mu} is the probability that the operation is conducted in the k^{th} dimension of thej^{th} particle.

Use the Sigmoid function to normalize the speed obtained by (14), given by (15).

$$S(v_{jk}(t+1)) = \text{sig}(v_{jk}(t+1)) = \frac{1}{1 + \exp(-v_{jk}(t+1))} \tag{15}$$

where $S(v_{jk}(t))$ represents the probability that the k^{th} dimension of the j^{th} particle changes from one state to another at the t^{th} iteration. Each particle updates the position vector according to (16).

$$Y_{jk}(t+1) = \begin{cases} 1, & \text{if } R_{4k}(t) < S(v_{jk}(t+1)) \\ 0, & \text{otherwise} \end{cases} \tag{16}$$

where $R_{4k}(t)$ indicates the random number between 0 and 1.

The BPSO algorithm steps are as follows:

Step 1: Initialize particle population, including initialization of particle position and velocity.

Step 2: Calculate the fitness value of the first-generation particle by (9).

Step 3: Update the personal best Y_P and global best Y_G according to the return value of the fitness function.

Step 4: Update particle speed by (11), (13), and (14), then update the particle position by (15).

Step 5: Calculate the fitness value of the current-generation particle by (9).

Step 6: Update the personal best Y_P and global best Y_G according to the return value of the fitness function.

Step 7: If $t = T_{\max}$, it ends and output global best Y_G. Otherwise, go to step 4.

III. SIMULATION AND COMPARISON

A. DIRECTIVITY DIAGRAM

Taking 64-element full array transducer as an example, the element layout of the linear sparse phased array was optimized by the proposed method. For comparison purposes, another full array with the same number of elements as the optimized sparse array is also calculated. The full array transducer parameters are shown in Table 1, where the parameters

TABLE 1. The full array parameters.

Element width	0.53 mm
Element pitch	0.63 mm
Central frequency	5 MHZ
Sound velocity	6300 m/s
Bandwidth (-6 dB)	50%

satisfy $d = \frac{\lambda}{2}$ to prevent the generation of periodic grating lobes, λ is the wavelength.

According to the reasonable selection range of the parameters, the size of the initial population group was set to 50 after several attempts, the number of iterations was set to 200, and r_{mu} set to 0.2. And carry out simulation experiments with Matlab software, then the directivity diagrams of the 64-element full array and the optimized sparse array are shown in Fig.3 (a) and Fig.3 (b), respectively.

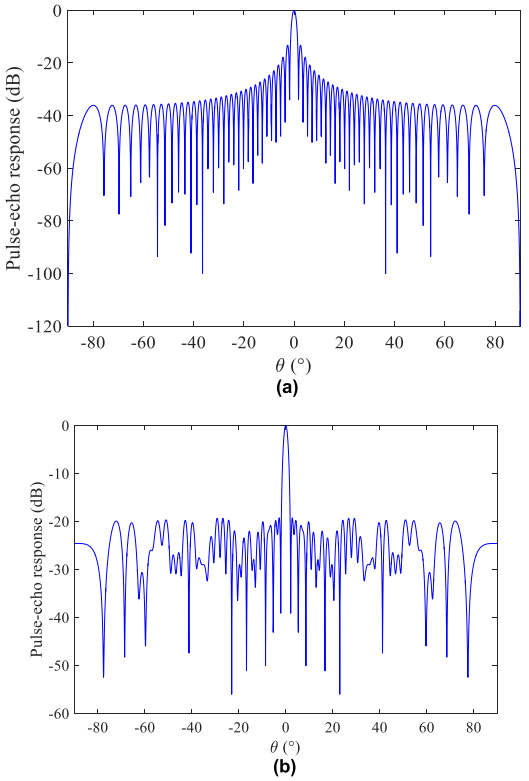

FIGURE 3. The directivity diagram of (a) 64-element full array and (b) optimized sparse array.

In the directivity diagram of 64-element full array, there are large sidelobes around the main lobe. The MSL and MLW are −13.2455dB and 2.1557°, respectively. In the optimized sparse array, the sidelobes suppression effect is obvious, the MSL is -19.0035dB, and the MLW of −6dB is 2.4620°. The MSL decreased by 5.758dB, but the MLW was slightly widened. The convergence curves of the fitness value of the optimization process by GA and BPSO are shown in Fig. 4.

It can be seen from Fig. 4 that the minimum fitness value obtained by using BPSO is significantly lower than that of GA. The minimum fitness value was 1.59 lower in the former than in the latter. It can be seen that the BPSO is used to converge faster and the optimization effect better. Therefore, it is feasible to use the BPSO as an optimization method for one-dimensional sparse arrays. It can be seen from the convergence curve of BPSO that compared with the reference full array, the final fitness value is down to approximately −16.8617, which is the sum of the MSL and the MLW of −6dB of the optimized sparse array. The array layout of the optimized sparse array is "010111000110 0110111111111111111111111111010111111111101101011". The number of array elements has been reduced by 13, which will greatly improve the FMC/TFM efficiency. For comparison purposes, we plotted the directivity diagram of the full array with the same number of elements as the optimized sparse array, the array parameters are also the same as those in Table 1. The directivity diagram of the 51-element full array is shown in Fig.5.

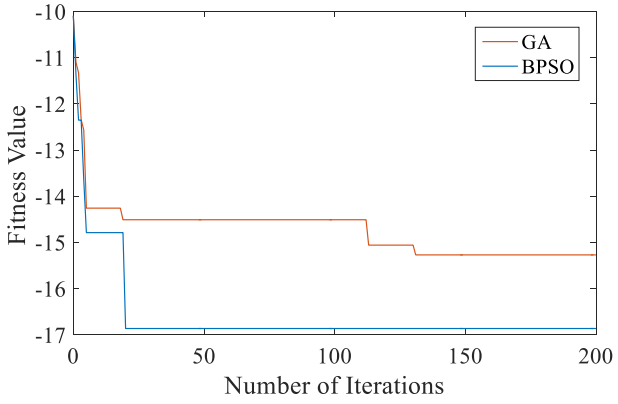

FIGURE 4. The fitness value with iterations of two algorithms.

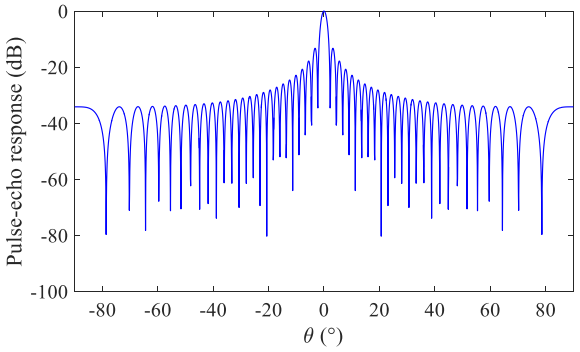

FIGURE 5. The directivity diagram of the 51-element full array.

Compared with the 64-element full array, the MSL is almost invariable in Fig.5, but the MLW is significantly increased. By measurement, the MSL and MLW of −6dB of the 51-element full array are −13.2476 dB and 2.7064°, respectively. As the number of elements of the full array decreases by 13, the MLW increases by 0.5507°. This is very natural because the reduction of the number of array elements will inevitably lead to the reduction of the size of the effective aperture of the full array transducer. However, the optimized sparse array is obtained based on the full array

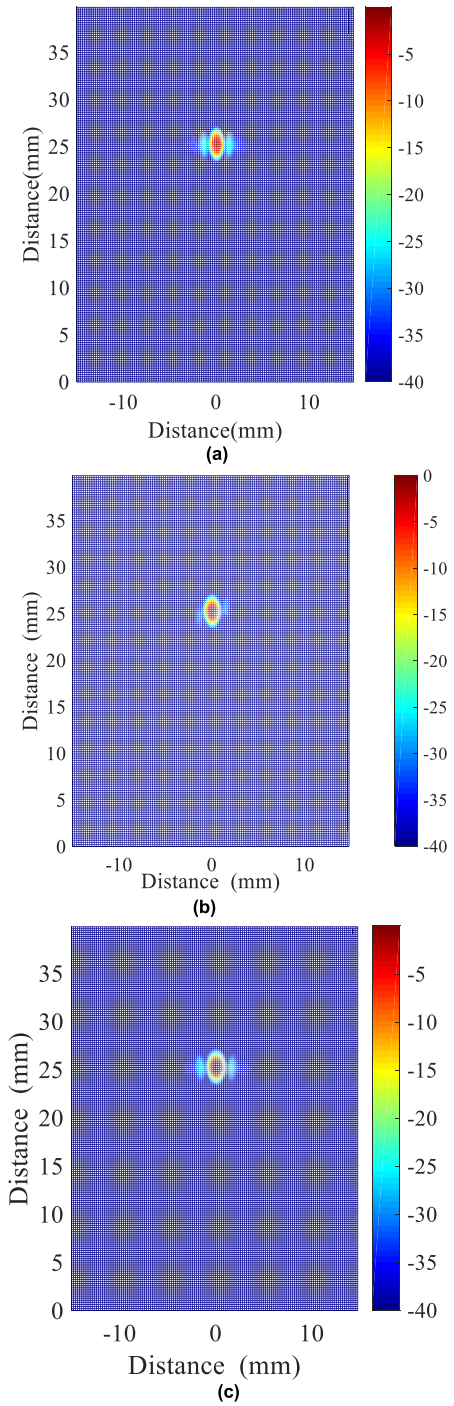

FIGURE 6. TFM images of a point-like scatter using different arrays. (a) 64-element full array; (b) optimized sparse array; (c) 51-element full array.

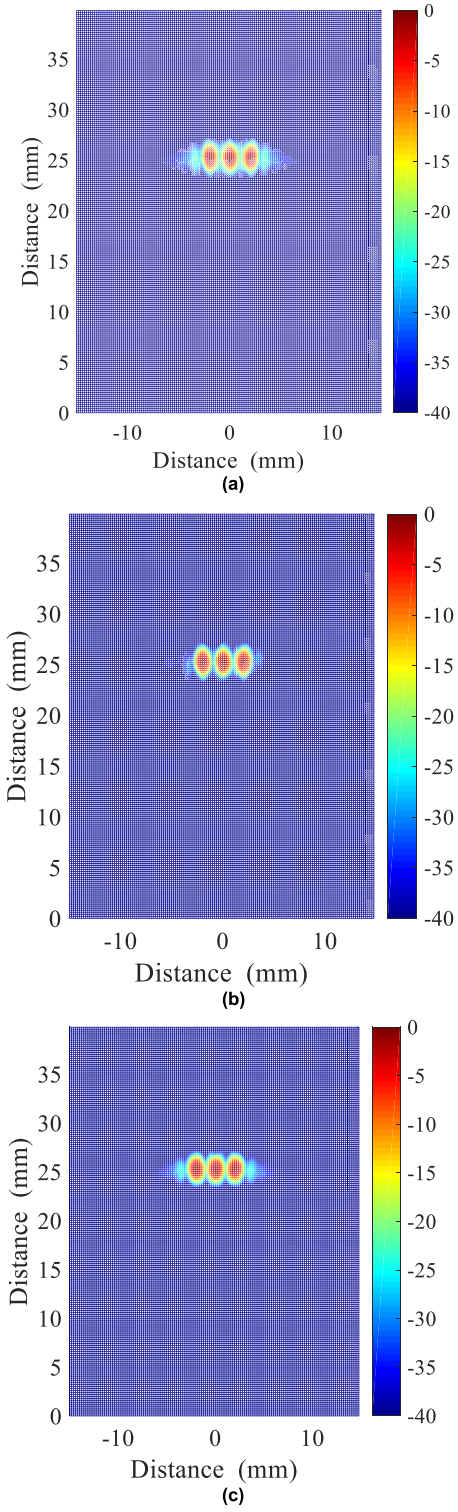

FIGURE 7. Images of three point-like scatters using different arrays. (a) 64-element full array; (b) optimized sparse array; (c) 51-element full array.

by minimizing fitness value, which guarantees the size of the effective aperture so that imaging resolution hardly affected.

B. TFM

To verify the TFM effect of optimized sparse arrays, a simulation by MATLAB was performed to compare these three arrays mentioned above. The point spread function (PSF) is the response of the imaging algorithm to a single ideal scattering point. In a linear sound field, the imaging result of any defect can be regarded as the convolution process of the actual scattering function of the defect and PSF [20]. Therefore, in this paper, we use PSF to characterize the spatial imaging characteristics of the TFM algorithm.

TABLE 2. The performance of the different array.

Array distribution	MLW(°)	MSL(dB)	API	SNR (dB)	Run time consumed (s)
32-element full array	4.3165	-13.2367	1.0793	39.9074	11.0625
optimized sparse array (26-element)	5.0219	-18.8563	1.2354	39.9432	8.8729
26-element full array	5.3145	-13.2151	1.3028	39.8975	8.7206
96-element full array	1.4353	-13.2914	0.4289	39.8779	57.4301
optimized sparse array (71-element)	1.6703	-19.4831	0.4870	39.9351	43.5452
71-element full array	1.9433	-13.2474	0.5627	39.9005	40.2343
128-element full array	1.0746	-13.2567	0.3461	39.8051	99.1693
optimized sparse array (88-element)	1.2397	-19.5638	0.3786	39.8949	67.6255
88-element full array	1.5678	-13.2479	0.4615	39.8781	65.4806

The full array parameters are in Table 1. The array element distribution of the sparse array is determined based on the optimization results of the directivity diagram above. The output of each element was a five cycle, Gaussian windowed tone burst with a 5 MHz center frequency and a −6 dB bandwidth of 50%. Fig. 6 shows the results scaled in dB to display a point-like scatter at $(0, 20\lambda)$ after the generation of pixels based on the FMC signals. The imaging area is 30 mm × 40 mm. It is divided into a 0.2 mm grid on the horizontal and vertical axes, and the grid size is 150 × 200 pixels.

As can be seen from the Fig.6, in the imaging area of the 64-element full array and the 51-element full array, there are ''ear'' shaped areas on both sides of the ideal point oval area, which is generated by the side beam lobe scanning. And the size of the point defect of the 51-element full array is larger than that of the 64-element full array. Interestingly, the artifacts of optimized sparse array imaging almost disappeared, and single-point defects were clearer, the size of the point defect is close to that of the 64-element full array. The imaging effects of the three arrays are consistent with the theoretical analysis of their corresponding directivity diagram synthetic beams.

For the purpose to evaluate quantitatively the imaging performance of the array, we need to introduce the array performance indicator. SNR and imaging resolution and are the main criteria for measuring the performance of ultrasound imaging methods.

The SNR is the ratio of the reflected signal power to the noise power in imaging. We measure the SNR of the image by calculating the ratio of the peak amplitude $I_{\max}$ of the defect location to the average amplitude A_{average} of the non-defective area in the background portion of the image, and the unit is converted into decibels, the SNR is given by

$$SNR = 20\log_{10}\left|\frac{I_{\max}}{A_{\text{average}}}\right| \tag{17}$$

Imaging resolution includes vertical and horizontal resolution. The vertical resolution is related to the center frequency and bandwidth of the transducer, and the horizontal resolution is mainly determined by the main-lobe width of the emission beam. For the purpose to evaluate quantitatively the imaging resolution of the array, we introduce the Array Performance Indicator API [13], which is given by

$$API = \frac{A_{-6\text{dB}}}{\lambda^2} \tag{18}$$

where $A_{-6\text{dB}}$ is the area of the PSF which is greater than −6dB down from its maximum value. The smaller the API, the better the imaging resolution of the array.

By calculating, the API in Fig. 6 (a),(b),(c) are 0.6160, 0.6595, and 0.7180, respectively, and the SNR are 39.9085 dB, 39.9452 dB, and 39.9125 dB, respectively. The optimized sparse array has the highest SNR and has a smaller API value than the 51-element full array. What is more, in the whole simulation process, the imaging time of the optimized sparse array is reduced by more than 20% compared with the 64-element full array. which means the sparse array can improve the efficiency of ultrasonic detection. Although the API of the optimized sparse array is slightly increased than the reference full array. On the one hand, the error is small, which guarantees image resolution of the sparse array close to that of the reference full array. On the other hand, the performance of the optimized sparse array can be biased toward the resolution by changing the coefficient ψ_1, ψ_2 of the fitness function according to the actual situation.

To study the imaging performance of the three arrays for the closely spaced scatterers, we set up three point-like scatters with a spacing of 2mm. i.e., the scatter positions are $(-1.59\lambda, 20\lambda)$, $(0, 20\lambda)$, and $(1.59\lambda, 20\lambda)$, respectively. The TFM results of three arrays as shown in Fig.7.

It can be seen from Fig. 7 that the 64-element full array has the strongest sidelobe energy near the main lobe, and the obvious artifacts. The ellipse-shaped image area at the point-like scatters of the 51-element full array is the biggest, which indicates that it has the lowest lateral resolution within the three arrays. Interestingly, The imaging quality of the optimized sparse array with three point-like scatters is also very great, the artifacts near the defect points are significantly reduced, and the scatter outline is visible clearly. Some 1D patterns extracted from Fig.7 are plotted in Fig. 8,

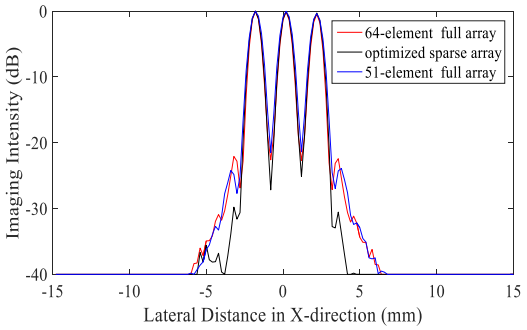

FIGURE 8. The simulated imaging intensity distribution in the lateral direction in comparison to that with the full array.

which are distributed along the lateral direction and crossing the mainlobe peak point.

Peak to Centre Intensity Difference represents the level of pixel peak drop in the x-direction at the depth of the z-axis where two adjacent scatterers are located in the image, which is recorded as ΔA. In Fig.8, we found that the horizontal width of the mainlobe of three arrays is very close to each other, but the ΔA of the optimized sparse array is minimum, which indicates that two adjacent scatterers can be better distinguished. And the sparse array has the lowest side beams of three array, so there are fewer imaging artifacts and a higher SNR.

C. THE PERFORMANCE OF DIFFERENT ARRAY

To study the generality of the proposed method, we calculated the imaging performance of several one-dimensional full arrays with different numbers of array elements, corresponding optimized sparse arrays, and the full array with the same number of array elements as the optimized sparse arrays. The array parameters are the same as those of the above example array. The time-consuming is measuring with the processor identified by Intel(R) Core(TM) i7-8750 CPU @2.20GHz and the runtime environment is MATLAB R2015b. The results are shown in Table 2, which can be summarized as follows.

1). Although the number of elements in the reference full array is different, the optimized sparse array always has a lower MSL and higher SNR than that of the corresponding reference full array. When the number of array elements is the same, compared with the full array, the sparse array has lower MSL, lower API, and higher SNR.

2). The run time consumed by FMC/TFM simulation is proportional to the number of array elements. The sparse array has less time than the reference full array.

3). The total size of the active elements of the optimized sparse array is about 0.7 of the reference full array aperture.

4). In general, as the number of elements of the full array increases, both the API and the SNR are decreases. However, through optimization by BPSO, the imaging SNR can be improved to a certain extent for each reference full array.

In short, no matter how many the number of elements in the reference full array, the optimized sparse array can improve the imaging SNR. Although the imaging resolution of the array is slightly reduced after optimization, the imaging efficiency can be improved, the method is feasible.

TABLE 3. The nomenclature.

Notations	Descriptions
x_i , x_j	The i^{th} and j^{th} element
x_n , z_m	The x-axis and z-axis coordinate of the scattering point P
r_{iP} , r_{jP}	Distance from point P to the i^{th} and j^{th} element
$u(x_i,x_j,t)$	The data collected of by the full matrix
t_{ijP}	The acoustic propagation delay
c	The longitudinal velocity of sound
h_{ij}	The analytical version of the echo received signal
I	The pixel intensity value
p	Sound pressure
r	The distance between the imaging point and the array element
k	Wave number
p_0	A function of the wave number
θ	Direction angle
ω	Circular frequency
a	Element width
g_i	The i^{th} binary coefficient
θ_m	The steering angle of the phased array
H	Beam directivity function
ψ_1 , ψ_2	Coefficient of optimization objective
Fit	Fitness value
MSL	The maximum sidelobe level
MLW	The main-lobe width (-6dB)
Y_{jk}	The value of the k^{th} dimension of the j^{th} particle
v_{jk}	The speed of the k^{th} dimension of the j^{th} particle
$R_{1k}, R_{2k}, R_{3k}, R_{4k}$	The random number between 0 and 1
$w, w_{\max}, w_{\min}$	Inertia coefficient
c_1 , c_2	Acceleration factor
r_{mu}	Selection factor
Y_P	Personal best
Y_G	Global best
λ	The wavelength
d	Element pitch
a	Element width
SNR	Signal noise ratio
A_{average}	The average amplitude of the nondefective area of the image
API	The array performance indicator
$A_{-6\text{dB}}$	The area of the PSF which is greater than -6dB down from its maximum value
ΔA	Peak to centre intensity difference

IV. CONCLUSION

This paper introduces a design method of the sparse array. Based on the reference full array, the BPSO is used to automatically sparsify the array by calculating phased array

patterns. Finally, the array is sparse to a suitable level without reducing the sound field characteristics. On the whole, the optimized sparse array has better performance than the reference full array. The ultrasonic imaging results by TFM indicate that the optimized sparse array not only has better imaging quality than the reference full array but also can improve the FMC/TFM efficiency. The method has certain universality and has certain reference values for the design of the phased array system. Future experimental validation will be performed to verify the imaging performance of sparse arrays. Further, apply this method to the optimal design of various phased array systems.

REFERENCES

[1] M. Karaman, I. O. Wygant, Ö. Oralkan, and B. T. Khuri-Yakub, "Minimally redundant 2-D array designs for 3-D medical ultrasound imaging," *IEEE Trans. Med. Imag.*, vol. 28, no. 7, pp. 1051–1061, Jul. 2009.

[2] P. B. Rosnitskiy, B. A. Vysokanov, L. R. Gavrilov, O. A. Sapozhnikov, and V. A. Khokhlova, "Method for designing multielement fully populated random phased arrays for ultrasound surgery applications," *IEEE Trans. Ultrason., Ferroelectr., Freq. Control*, vol. 65, no. 4, pp. 630–637, Apr. 2018.

[3] J. H. Hwang and L. A. Crum, "Current status of clinical high-intensity focused ultrasound," in *Proc. Annu. Int. Conf. IEEE Eng. Med. Biol. Soc.*, Minneapolis, MN, USA, Sep. 2009, pp. 130–133.

[4] L.-W. Kuo, L.-C. Chiu, W.-L. Lin, J.-J. Chen, G.-C. Dong, S.-F. Chen, and G.-S. Chen, "Development of an MRI-compatible high-intensity focused ultrasound phased array transducer dedicated for breast tumor treatment," *IEEE Trans. Ultrason., Ferroelectr., Freq. Control*, vol. 65, no. 8, pp. 1423–1432, Aug. 2018.

[5] A. Marzo, S. A. Seah, B. W. Drinkwater, D. R. Sahoo, B. Long, and S. Subramanian, "Holographic acoustic elements for manipulation of levitated objects," *Nature Commun.*, vol. 6, no. 1, Dec. 2015, Art. no. 8661.

[6] Y. Javadi, C. MacLeod, S. G. Pierce, A. Gachagan, D. Lines, C. Mineoa, J. Ding, S. Williams, M. Vasilev, E. Mohseni, and R. Su, "Ultrasonic phased array inspection of a wire + arc additive manufactured (WAAM) sample with intentionally embedded defects," *Additive Manuf.*, vol. 29, pp. 1–10, Oct. 2019.

[7] M. Dissanayake, D. Carswell, M. Corsar, T. P. Sattar, M. Sutcliffe, P. S. Lowe, and T.-H. Gan, "Automated application of full matrix capture to assess the structural integrity of mooring chains," *IEEE Access*, vol. 6, pp. 75560–75571, 2018.

[8] L. Moreau, B. W. Drinkwater, and P. D. Wilcox, "Ultrasonic imaging algorithms with limited transmission cycles for rapid nondestructive evaluation," *IEEE Trans. Ultrason., Ferroelectr., Freq. Control*, vol. 56, no. 9, pp. 1932–1944, Sep. 2009.

[9] H. Peng, J.-P. Peng, H.-N. Zhu, Z.-Y. Wang, and X.-R. Gao, "The efficiency optimization of full matrix capture imaging detection based on increasing the effective aperture," in *Proc. IEEE Far East Forum Nondestruct. Eval./Test.*, Chengdu, China, Jun. 2014, pp. 50–56.

[10] P. Chen, Y. Zheng, and W. Zhu, "Optimized simulated annealing algorithm for thinning and weighting large planar arrays in both far-field and near-field," *IEEE J. Ocean. Eng.*, vol. 36, no. 4, pp. 658–664, Oct. 2011.

[11] H. Hu, J. Du, N. Xu, H. Jeong, and X. Wang, "Ultrasonic sparse-TFM imaging for a two-layer medium using genetic algorithm optimization and effective aperture correction," *NDT & E Int.*, vol. 90, pp. 24–32, Sep. 2017.

[12] M. G. Bray, D. H. Werner, D. W. Boeringer, and D. W. Machuga, "Optimization of thinned aperiodic linear phased arrays using genetic algorithms to reduce grating lobes during scanning," *IEEE Trans. Antennas Propag.*, vol. 50, no. 12, pp. 1732–1742, Dec. 2002.

[13] P. Yang, B. Chen, and K.-R. Shi, "A novel method to design sparse linear arrays for ultrasonic phased array," *Ultrasonics*, vol. 44, pp. e717–e721, Dec. 2006.

[14] G. R. Lockwood, P.-C. Li, M. O'Donnell, and F. S. Foster, "Optimizing the radiation pattern of sparse periodic linear arrays," *IEEE Trans. Ultrason., Ferroelectr., Freq. Control*, vol. 43, no. 1, pp. 7–14, Jan. 1996.

[15] Y. Lavadi, E. Mohseni, C. N. MacLeod, D. Lines, M. Vasilev, C. Mineo, E. Foster, S. G. Pierce, and A. Gachagan, "Ultrasonic phased array inspection of a wire + arc additive manufactured (WAAM) sample with intentionally embedded defects," *Mater. Des.*, vol. 191, pp. 1–29, Jun. 2020.

[16] J. Peng, H. Peng, Y. Zhang, X. Gao, C. Peng, and Z. Wang, "Study on the railway wheel ultrasonic inspection method using the full matrix capture," in *Proc. Far East Forum Nondestruct. Eval./Test., New Technol. Appl.*, Jinan, China, Jun. 2013, pp. 118–124.

[17] S.-C. Wooh and Y. Shi, "Optimum beam steering of linear phased arrays," *Wave Motion*, vol. 29, no. 3, pp. 245–265, Aug. 1999.

[18] L. A. Greda, A. Winterstein, D. L. Lemes, and M. V. T. Heckler, "Beam-steering and beamshaping using a linear antenna array based on particle swarm optimization," *IEEE Access*, vol. 7, pp. 141562–141573, 2019.

[19] H. Li, Y. Jiang, Y. Ding, J. Tan, and J. Zhou, "Low-sidelobe pattern synthesis for sparse conformal arrays based on PSO-SOCP optimization," *IEEE Access*, vol. 6, pp. 77429–77439, 2018.

[20] J. Zhang, B. W. Drinkwater, and P. D. Wilcox, "Comparison of ultrasonic array imaging algorithms for nondestructive evaluation," *IEEE Trans. Ultrason., Ferroelectr., Freq. Control*, vol. 60, no. 8, pp. 1732–1745, Aug. 2013.

HAN ZHANG received the Ph.D. degree from the Chinese Academy of Sciences, Beijing, China, in 2009.

She was a Visiting Scholar (Advisor: J. D. Achenbach) with Northwestern University, Evanston, IL, USA. She is currently an Associate Professor with the Institute of Acoustics, Chinese Academy of Sciences. Her current research interests include vibration and wave propagation with passive and active structures and their applications in acoustic meta materials, energy harvesting, non-destructive testing, structural health monitoring, particle manipulation, and acoustic communication.

BICHAO BAI received the B.S. degree in electronic information engineering from the Huaide College, Changzhou University, China, in 2018, where he is currently pursuing the M.S. degree with the School of Mechanical Engineering.

His research interests include ultrasound focus and array signal processing.

JIANFENG ZHENG received the B.Eng. degree from the Jiangsu Institute of Petrochemical Technology, Changzhou, China, in 2000, and the M.Sc. degree from the Nanjing University of Science and Technology, Nanjing, China, in 2012.

He has been with the School of Mechanical Engineering, Changzhou University, since 2000, where he was an Associate Professor, in 2016. His current research interests include detection and control of smart grid high-voltage equipment and embedded control of the intelligent instrument.

YUN ZHOU received the B.S. degree in electrical engineering and automation from Nanjing Normal University, in 2017. He is currently pursuing the M.E. degree with the School of Mechanical Engineering, Changzhou University, China.

His research interest includes ultrasonic wireless power transmission.